*Article*

# Fractal Dimension Analysis of Structure and Bending Strength of Porous Alumina Prepared Using Starch and Carbon Fiber as Pore-Forming Agents

Chang Chen [1,*], Xuecheng Ding [1], Yubin Wang [2], Zhixing Luo [3] and Peiyu Zhai [1]

[1]  College of Materials Science and Engineering, Xi'an University of Architecture and Technology, Xi'an 710055, China
[2]  School of Resources Engineering, Xi'an University of Architecture and Technology, Xi'an 710055, China
[3]  College of Architecture, Xi'an University of Architecture and Technology, Xi'an 710055, China
*   Correspondence: changchen420@xauat.edu.cn

**Abstract:** Porous alumina was prepared via a sacrificial template method using alumina as the matrix and starch and carbon fibers as the pore-forming agents. After sintering, no residual pore-forming agents were present. The density, porosity, and pore structure of the samples were measured using the Archimedes' method and mercury intrusion porosimetry (MIP). The results showed that the pore size distribution of porous alumina was double-peak when the content of the pore-forming agent was 20, 30, or 50 vol.%, but was single-peak when the content was 40 vol.%. A fractal model based on the measured MIP data was used to calculate and evaluate the fractal dimension ($D_s$) of porous alumina. The $D_s$ values decreased with an increase in the pore-forming agent content. Furthermore, $D_s$ was negatively correlated with porosity, most probable pore size, and median pore diameter and positively correlated with the bending strength of porous alumina. Since porous alumina has obvious fractal characteristics, the fractal theory can be used to quantitatively describe its complex distribution.

**Keywords:** porous alumina; starch; carbon fiber; pore structure; bending strength; fractal dimension

## 1. Introduction

Recently, porous ceramics have become of great interest in porous material research because of their excellent filtration, adsorption, and desorption capabilities, high-temperature resistance, oxidation resistance, thermal shock resistance, and chemical corrosion resistance [1–5]. They are widely used in sensors, filters, molten metals, catalyst carriers, refractories, and biomedical materials [6–13]. Additionally, alumina is one of the most widely used ceramic materials because of its high strength, hardness, wear resistance, etc. [14–17]. Nevertheless, the particle diffusion coefficient of alumina is low because of its strong ionic bond ($Al^{3+}$ diffusion coefficient is only $10^{-11}$ $cm^2/s$ at 1700 °C), and its sintering temperature is higher than 1500 °C [18,19]. Sintering additives are used to reduce the sintering temperature but can also serve as pore-forming agents.

The sacrificial template method is one technique used to prepare porous ceramics. In this approach, an appropriate amount of pore-forming agent is mixed with ceramic powder. The pore-forming agent is then removed by evaporation or combustion before or during sintering so that pores remain in the ceramic body [20,21]. Specific pore structures can be obtained using the sacrificial template method [22]. Starch is a type of polysaccharide composed of amylose and amylopectin produced by plant photosynthesis. It is often used as a biological pore-forming agent in ceramic technology because it easily burns away at low temperatures and leaves no residue after sintering [23–26]. With the rapid development of fiber materials, some researchers also use fibers as a pore-forming agent to prepare porous materials. Zao et al. [27] prepared porous ceramics with a connecting channel structure using polypropylene fibers (diameter of 120 μm and length of approximately 4 mm) as

pore-forming agents, and the fibers were decomposed in a sintered body to form connecting channels with a diameter of 100 μm. Corradetti et al. [28] successfully prepared lanthanum carbide targets with enhanced permeability using 21.3 vol.% nylon 6/6 and 24.8 vol.% polypropylene (average length of 500 μm and diameter of 18 and 20 μm, respectively) as pore-forming agents. Biggemann et al. [29] successfully fabricated alumina ceramics with multimodal pore networks using pyrolytic cellulose fibers (length of 150 μm and diameter of 8 μm) and two isotropic phenolic resin spheres (diameter of 30 and 300 μm) as pore-forming agents. The results showed that the type of sacrificial template is the main factor affecting the mechanical properties of alumina ceramics. The properties of porous materials are influenced by the type, shape, and size of the fibers. Carbon fibers can be oxidized during the process of high-temperature sintering; thus, they can be discharged from the matrix while retaining the pores. Porous ceramics with high porosity and excellent performance can be prepared using carbon fibers with a large aspect ratio. Zhong et al. [30] prepared highly porous LAS/SiC ceramics using carbon fibers (average aspect ratio of 5) as the pore-forming agent and showed that overlapping carbon fibers could inhibit shrinkage due to drying.

The properties of porous ceramics are closely related to their pore structure. Presently, the main methods for pore structure characterization include scanning electron microscopy (SEM), nuclear magnetic resonance, nitrogen adsorption/desorption, and mercury intrusion porosimetry (MIP) [31,32]. Nevertheless, the pore structure of porous ceramics is complicated and irregular and is therefore difficult to describe by geometry. Fractal geometry is a new branch of mathematics used to solve the problem of irregular and fragmented patterns that cannot be analyzed by classical geometry. Since its establishment, more and more researchers have used the fractal theory to study the pore structure of materials; thus, the fractal dimension ($D_s$) is considered an important index to quantify pore structures [33–35]. The $D_s$, which is related to the macroscopic properties of materials, is calculated mathematically based on the MIP data and is a new index for characterizing pore structures [36–40].

In this paper, porous alumina ceramics were prepared by a sacrificial template method using alumina as the matrix and starch and carbon fiber as the pore-forming agents. The surface $D_s$ of porous alumina ceramics prepared using different pore-forming agent quantities was evaluated using the obtained MIP data. The influence of the pore-forming agent content on the physical properties, mechanical properties, and microstructure of porous alumina ceramics and the relationships between the surface $D_s$, the pore structure, and the mechanical properties were investigated in detail.

## 2. Materials and Methods

### 2.1. Raw Materials

An alpha-type calcined alumina powder (CT3000SG, Almatis GmbH in Ludwigshafen, Germany) with an average particle size of 0.5 μm and a specific surface area of 7.50 m$^2$/g was used as the ceramic phase. Different quantities (20, 30, 40, and 50 vol.%) of a starch and carbon fiber powder mixture (1:1 (*v/v*)) were added to the alumina powder as pore-forming agents for the preparation of porous materials (samples A, B, C, and D, respectively). The SEM images of the starch and carbon fibers are shown in Figure 1. The density of the starch at room temperature (25 °C), measured by a Helium pycnometer (AccuPyc 1330, Micromeritics GmbH, Unterschleißheim, Germany), was approximately $1.51 \times 10^6$ g/m$^3$, and the average diameter of the starch was 9.35 μm, as confirmed by light diffraction (Mastersizer S, Malvern Instruments Ltd., Worcesterhire, UK). The milled carbon fibers (Toho Tenax Europe GmbH in Wuppertal, Germany) had an average diameter of 7 μm and a length of 50–150 μm.
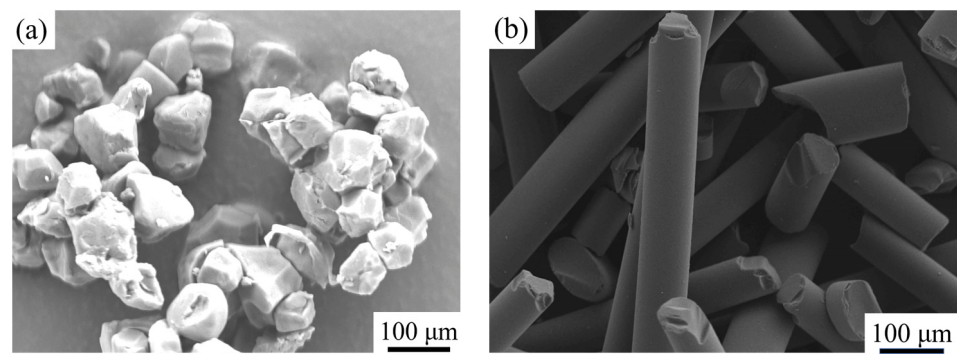
**Figure 1.** SEM photos of the pore-forming agents (**a**) starch and (**b**) carbon fibers.

### 2.2. Sample Preparation

Porous alumina ceramics were prepared by a sacrificial template method. The starch/carbon fiber ratio in the mixed powder was 1:1 (*v*/*v*). The raw material ratios of the different samples are shown in Table 1. For each sample, the alumina, starch, and carbon fiber mixture was wetted with ethanol and mixed in the ball mill for 24 h (using an $Al_2O_3$ grinding ball). The ethanol was then volatilized at a low temperature, and the sample was dried at 110 °C for 12 h in an electric blast drying oven. The dried mixed powder was screened using a 200-mesh screen, then put into a pressing mold (placed between the two pressing sheets between the upper and the lower pressing heads of the mold sleeve) and prepressed for 20 s with a rapid forming machine at 125 MPa for preliminary molding. The sample was then transferred into a cold isostatic pressure machine for molding at 500 MPa and finally placed in a muffle furnace for sintering. During the sintering process, combustion of the internal pore-forming agents took place, producing the porous $Al_2O_3$ ceramic material in situ.

**Table 1.** Ratios of the raw materials in the samples.

| Sample | Composition |
| --- | --- |
| A | 80 vol.% $Al_2O_3$ + 20 vol.% Starch and carbon fiber (1:1 *v*/*v*) |
| B | 70 vol.% $Al_2O_3$ + 30 vol.% Starch and carbon fiber (1:1 *v*/*v*) |
| C | 60 vol.% $Al_2O_3$ + 40 vol.% Starch and carbon fiber (1:1 *v*/*v*) |
| D | 50 vol.% $Al_2O_3$ + 50 vol.% Starch and carbon fiber (1:1 *v*/*v*) |

The dried mixed powder was tested by thermogravimetry–differential thermogravimetric analysis (DTA, STA409, Netzsch GmbH, Selb, Germany). The phase composition of the sintered sample was analyzed using a diffraction analyzer; then, the sample was ground and polished into a 3 mm × 4 mm × 50 mm sample. The cross-sectional morphology of the fractured samples was analyzed via SEM.

### 2.3. Sample Testing Methods

The density, total porosity, and open porosity of the samples were measured using the Archimedes' method and a glycerol solution according to ASTM C373–88. The four-point bending method was used to measure the bending strength in this experiment. The average density, porosity, and bending strength values of 10 samples in each batch were measured. The surface of the specimen was polished before the test to ensure that the upper and lower surfaces were parallel and the sample was chamfered. The sample size was 4 mm × 3 mm × 20 mm, the upper span was 10 mm, the lower span was 20 mm, and the loading rate was 0.5 mm/min. The surface microstructures were observed via SEM (LEO 1530 FESEM, Gemini/Zeiss, Oberkochen, Germany). The pore size distributions of the samples were determined using MIP (AutoPore IV 9500 V1.04, Micromeritics GmbH, Germany). Sample weights of 1.30–3.10 g were used for the measurements. The contact angle and surface tension used in the calculation were 141.3° and $485 \times 10^{-3}$ N/m, respectively.

### 2.4. Thermal Analysis

To study the physical and chemical changes during the sintering process in air, the initial combustion temperature and the final sintering temperature of the pore-forming agents were determined using DTA. Figure 2 shows the differential thermal changes of starch and carbon fibers during sintering. When the temperature was increased from room temperature, an endothermic peak occurred at approximately 100 °C due to the evaporation of a small amount of adsorbed water in the sample. With the temperature increase, two strong endothermic peaks occurred at 350 °C and 1000 °C, indicating the combustion of starch and carbon fibers, respectively, in air. After determining the combustion temperatures of the pore-forming agents, the sintering temperature of $Al_2O_3$ could be selected. According to Lapamnuayphon, the optimal sintering temperature of $Al_2O_3$ is 1550 °C.
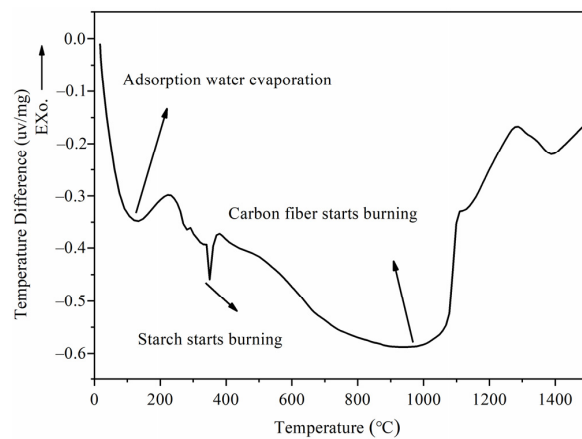


**Figure 2.** DTA curve for alumina with starch and carbon fibers.

## 3. Results and Discussion

### 3.1. Influence of the Pore-Forming Agent Content on Linear Shrinkage, Density, Porosity, and Weight Loss of Porous Alumina

Figure 3 shows the density, linear shrinkage, mass loss, and porosity of the samples sintered at 1550 °C using the Archimedes' method when the content of the pore-forming agents changed. The shape of the pore-forming agents (starch is polygonal granular, and carbon fibers are fibrous) affects the structure and properties of porous ceramics after sintering. For samples A–D, although the pore-forming agent content in the raw material mixture increased, the linear shrinkage rate remained at approximately 18%. This indicated that when starch and carbon fibers were used together as the pore-forming agents, the linear shrinkage rate was unaffected by the pore-forming agent content.
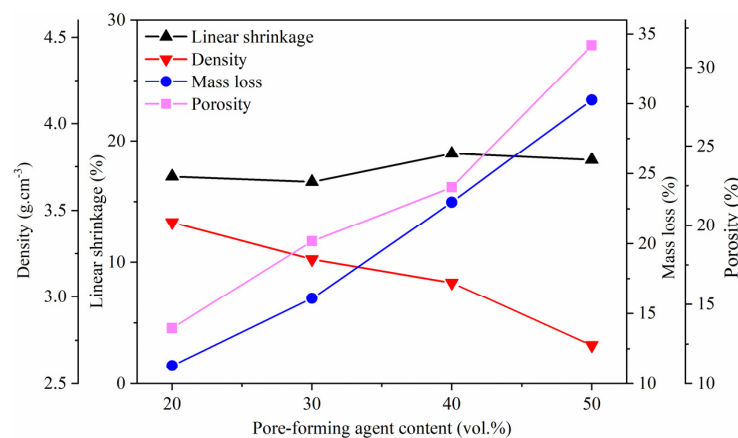


**Figure 3.** Density, linear shrinkage, mass loss, and porosity of porous alumina with different quantities of the pore-forming agent, sintered at 1550 °C.

The linear shrinkage values were consistent among different samples because the starch and carbon fiber were fully combusted at 1550 °C (as evidenced by the fact that the mass of the product equaled the mass of the alumina in the raw material mixture). However, the sample density decreased with an increasing pore-forming agent content because the mass of alumina in the mixture decreased. Similarly, the mass loss and porosity of the samples after sintering increased with an increase in the pore-forming agent content.

### 3.2. Effect of the Pore-Forming Agent Content on the Phase Composition and Microstructure of Porous Alumina

The XRD spectra of samples A–D are shown in Figure 4. Only typical diffraction peaks of $Al_2O_3$ appeared after the samples were sintered at 1550 °C for 2 h, indicating that the pore-forming agents in all of the samples were completely removed during the sintering process.
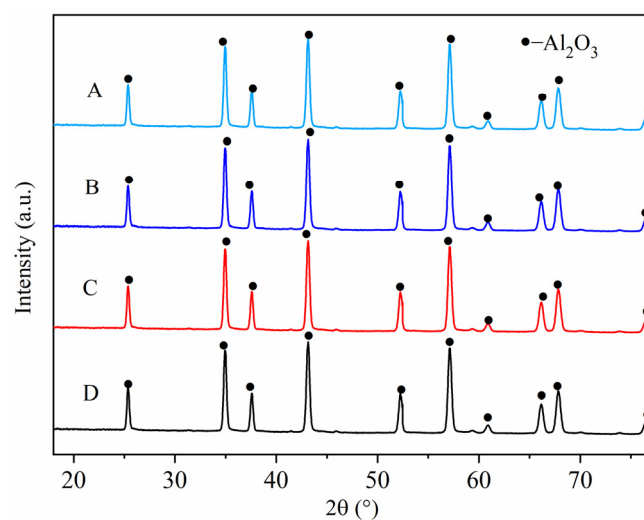


**Figure 4.** XRD patterns of the samples sintered at 1550 °C, composed of (**A**) 20 vol.% pore-forming agents + 80 vol.% alumina, (**B**) 30 vol.% pore-forming agents + 70 vol.% alumina, (**C**) 40 vol.% pore-forming agents + 60 vol.% alumina, and (**D**) 50 vol.% pore-forming agents + 50 vol.% alumina.

The SEM images of the porous alumina samples obtained by adding different quantities of the pore-forming agents are shown in Figure 5. As shown in Figure 5(A1), the $Al_2O_3$ fracture morphology of the sample prepared using 20 vol.% pore-forming agents and 80 vol.% alumina mainly included transgranular and intergranular fractures. We observed that in the $Al_2O_3$ phase of the transgranular fracture, the gaps between the particles were not filled completely during the sintering process, and closed pores with sizes of 0.26–0.74 μm formed. Additionally, because the size of the pore-forming agent powder was much larger than that of the $Al_2O_3$ particles, the contact surfaces between the $Al_2O_3$ particles were relatively large during the sintering process, which promoted liquid phase sintering on the surface. Therefore, part of the $Al_2O_3$ particles in the sintered sample increased in size to 0.50–6.00 μm. For the morphology of the cutting surface (Figure 5(A2)), Image J software was used to analyze the sample, with an average aperture of approximately 6.00 μm. Based on the linear shrinkage rate calculation and the diameter of the pore-forming agent particles, the pore size of the sample was 5.32–7.67 μm, indicating that the measured and calculated results were in good agreement. Moreover, the fracture morphology of $Al_2O_3$ was mainly transformed from transgranular and intergranular fracture to intergranular fracture, as shown in Figure 5(B1,C1,D1). Because the porosity of the porous $Al_2O_3$ ceramics increased, the samples were easily fractured. Meanwhile, the diameter of the $Al_2O_3$ particles in the samples was 0.50–3.00, 0.50–2.00, and 0.50–1.00 μm, as shown in Figure 5(B1,C1,D1), respectively. With the increase in the pore-forming agent content, the contact surface of the raw $Al_2O_3$ particles decreased correspondingly, resulting

in no increase in the $Al_2O_3$ particle size in sample D. Thus, with the increase in the pore-forming agent content, the size of the $Al_2O_3$ ceramic particles decreased correspondingly. The higher the pore-forming agent content, the greater the distances between the $Al_2O_3$ ceramic particles during the sintering process, which was not conducive to the growth of the $Al_2O_3$ ceramic particles. The pore size analysis of the fracture surfaces of the samples in Figure 5(B2,C2,D2) was conducted using Image J software, and the average pore sizes were 6.40, 7.30, and 7.80 µm, respectively. As the pore-forming agent content in the raw material mixture increased, the content of starch and carbon fiber powder also increased. During the mixing process, the probability of contact or overlap between the carbon fiber and starch increased; thus, the average pore size obtained by sintering increased.
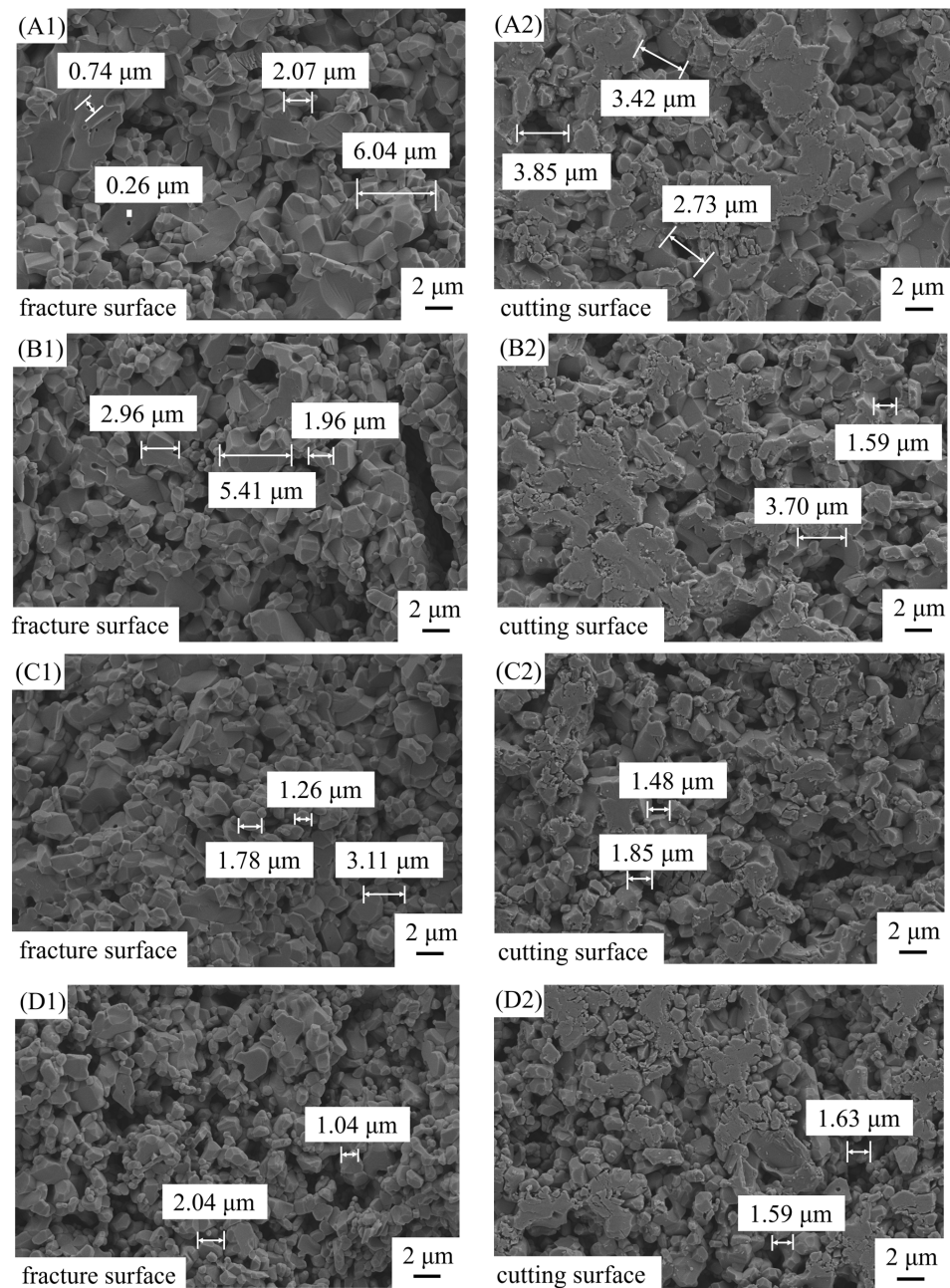


**Figure 5.** SEM images of the porous alumina prepared using different pore-forming agents. Agent contents: (**A1,A2**) 20 vol.% pore-forming agents + 80 vol.% alumina; (**B1,B2**) 30 vol.% pore-forming agents + 70 vol.% alumina; (**C1,C2**) 40 vol.% pore-forming agents + 60 vol.% alumina; (**D1,D2**) 50 vol.% pore-forming agents + 50 vol.% alumina.

### 3.3. Effect of the Pore-Forming Agent Content on the Pore Size Distribution of Porous Alumina

　　　The pore size distribution of the porous alumina samples (A–D) prepared with different quantities of the pore-forming agent is shown in Figure 6. For pore-forming agent contents of 20 vol.%, 30 vol.%, and 50 vol.%, the pore size distribution of porous alumina showed two peaks, which was caused by the size difference between the two pore-forming agents. The pore size distribution peaks appeared at 3 nm and 90 nm for sample A, 250 nm and 18 μm for sample B, and 500 and 900 nm for sample D. These pore size values were substantially smaller than those obtained by SEM analysis, which could be because MIP can only measure the pore size at the time of injection, and the pore shape of the samples were ink-bottle structures. In contrast, the pore size distribution of sample C was single-peak. This is because the pore distribution showed greater uniformity, and the pore size was more concentrated, as shown in Figure 5(C2). Additionally, at the sintering temperature of 1550 °C, the gaps between particles were completely occupied due to the diffusion of $Al_2O_3$ ceramic particles, and the holes left by the starch and the carbon fibers formed a mesh or an ink-bottle structure after sintering.
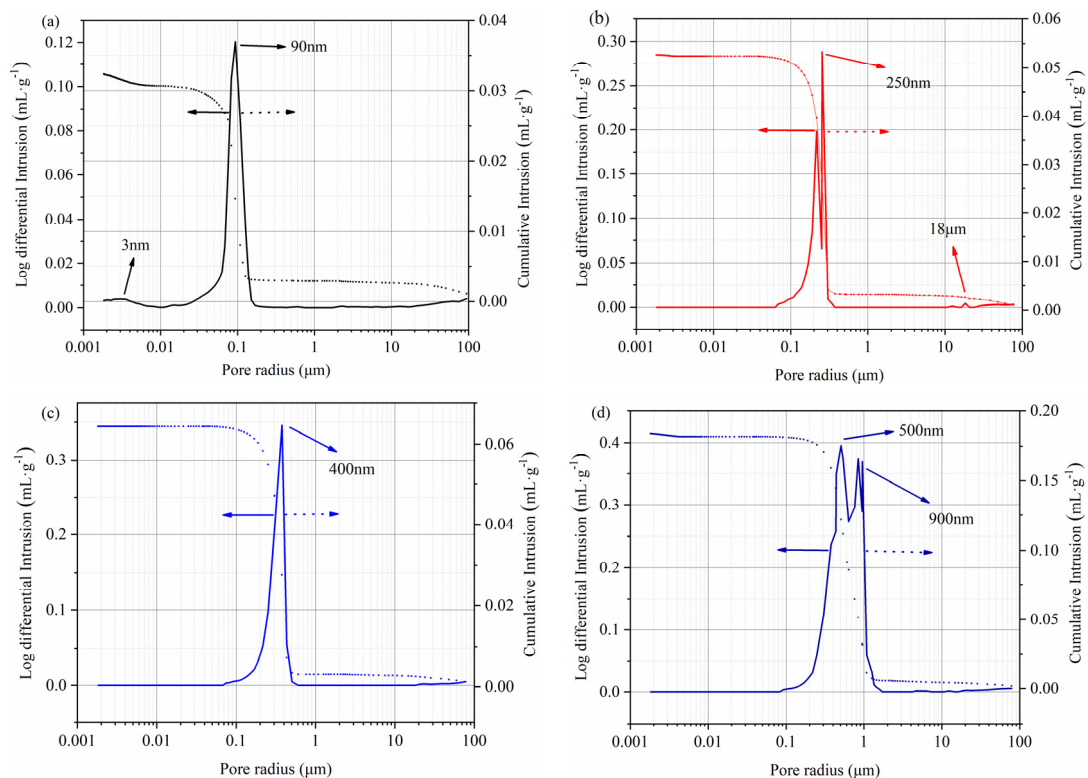


**Figure 6.** Pore size distribution of porous alumina with different quantities of the pore-forming agent, corresponding to (**a**) 20 vol.%, (**b**) 30 vol.%, (**c**) 40 vol.%, and (**d**) 50 vol.%.

　　　The physical properties of porous alumina measured by the Archimedes' method and MIP are shown in Figure 7, and the pore parameters measured by the MIP method are shown in Table 2. The total porosity and open porosity of the samples increased with the increase in the pore-forming agent content. The closed porosity of the samples decreased first and then increased with the increase in the pore-forming agent content. When the content of the pore-forming agents changed from 40% to 50%, the closed porosity of porous alumina increased due to the interlap of the fibrous carbon fibers. There was very little variation in porosity among the samples. However, the open porosity measured by MIP was higher than that measured by the Archimedes' method, indicating that MIP can be used to measure the volume of small pores with values closer to the real value.
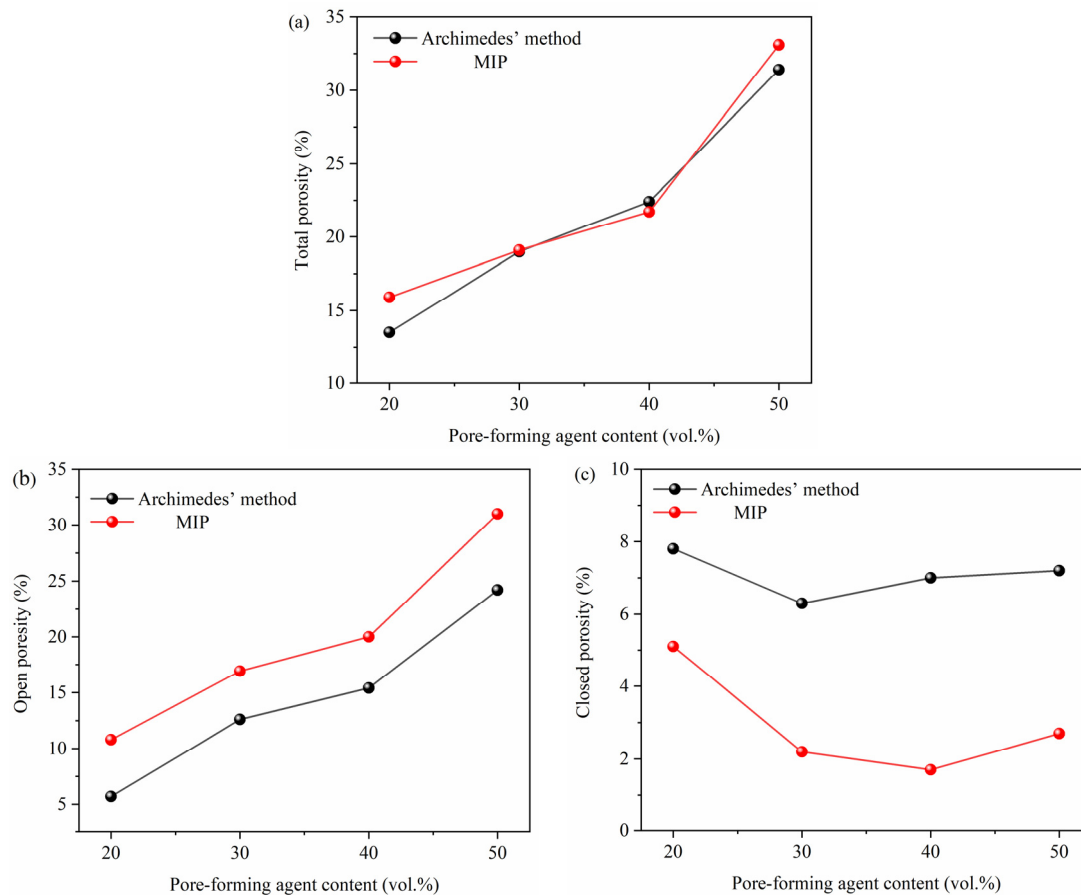
**Figure 7.** (**a**) Total porosity, (**b**) Open porosity, (**c**) Closed porosity of porous alumina measured using different testing methods.

**Table 2.** Pore structure parameters of porous alumina obtained by MIP.

| Sample | Pore Size Distribution (%) | | | |
|---|---|---|---|---|
| | **<10 nm** | **10–100 nm** | **100–1000 nm** | **>1000 nm** |
| A | 5.25 | 69.96 | 15.96 | 8.82 |
| B | 0.49 | 3.14 | 90.48 | 5.89 |
| C | 0.00 | 1.46 | 93.57 | 4.67 |
| D | 1.25 | 0.17 | 81.28 | 17.17 |

### 3.4. Mechanical Properties and Weibull Distribution of Porous Alumina

Figure 8 shows the relationship between bending strength and porosity for the sintered samples A–D. The bending strength of the sintered samples was 242, 168, 115, and 92 MPa when the pore-forming agent content was 20, 30, 40, and 50 vol.%, respectively. The size of the $Al_2O_3$ particles in the four sintered samples was quite similar. As the pore size in the samples increased, the ability of porous alumina ceramics to resist bending deformation decreased. The relationship between bending strength and porosity can be described using the Ryskewitsch equation $[\sigma_f = \sigma_0 \times exp(-np)]$, in which the theoretical bending strength value ($\sigma_0$) was 605 MPa, and the empirical constant ($n$) was 6.9.

The Weibull distribution of the porous alumina samples prepared with different pore-forming agent contents is shown in Figure 9. The ceramic materials differed according to the different raw materials, crack size, and shape. Even for a batch of samples, the mechanical properties differed under the same experimental conditions. Generally, the Weibull coefficient ($m$) value of ceramic materials (including porous ceramics) is in the range of 5–30, with 10–20 being the most common measured value. The larger the $m$ value,

the smaller the deviation in its strength data, and the higher the reliability or measured strength of the material. The calculated *m* values for samples A–D were 12.2, 15.9, 19.6, and 18.7, respectively, within the typical range of porous ceramics.
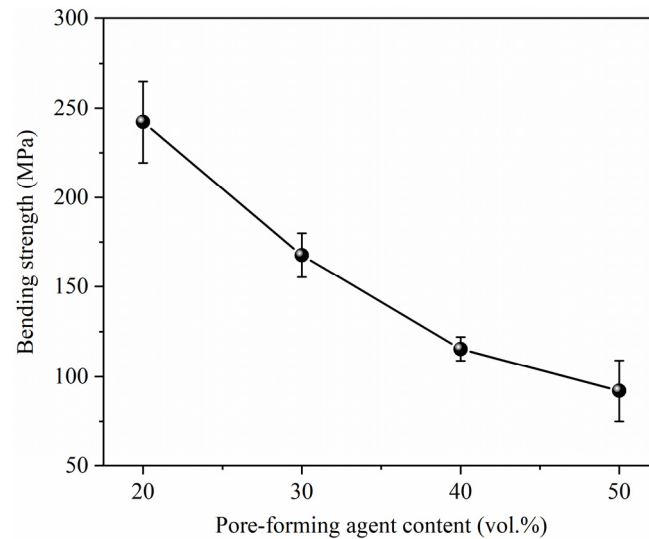


**Figure 8.** Relationship between the bending strength of porous alumina and the content of the pore-forming agents.
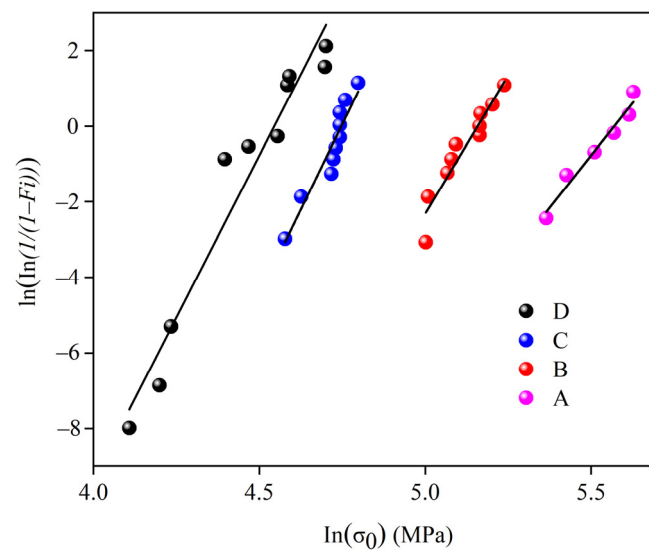


**Figure 9.** Weibull distribution of porous alumina prepared using different contents of the pore-forming agents.

### 3.5. Fractal Characteristics of Porous Alumina

To describe the pore structure and its effect on the mechanical properties of porous ceramics accurately, the fractal theory was used to calculate the $D_s$ values of the porous surfaces. The principle of Zhang and Li's fractal model is similar to the detection principle of MIP, which makes this model reliable and widely used [41]. The Zhang and Li's model is based on the energy conservation relationship in the MIP test, which is the logarithmic relationship between the cumulative intrusion work ($W_n$) and the cumulative mercury intrusion surface ($Q_n$), as shown in Equations (1)–(3).

$$\ln(W_n) = C + \ln(Q_n) \quad (1)$$

$$W_n = \sum_{i}^{n} P_i \Delta V_i \tag{2}$$

$$Q_n = r_n^{2-D} V_n^{D/3} \tag{3}$$

Here, $D$ is the actual pore surface size, $n$ is the number of mercury injections as determined by MIP, $P_i$ is the pressure at the $i$th injection of mercury, and $V_i$ is the volume of the mercury injected at the $i$th mercury injection. Equations (1)–(3) can be arranged into Equation (4) as follows:

$$\ln\left(\frac{W_n}{r_n^2}\right) = D_s \ln\left(\frac{V_n^{1/3}}{r_n}\right) + C \tag{4}$$

The values of $W_n$, $V_n$, $\ln\left(\frac{W_n}{r_n^2}\right)$, and $\ln\left(\frac{V_n^{1/3}}{r_n}\right)$ can be calculated according to the MIP detection results and Equations (2) and (3). From these values, a fitting curve for Equation (1) can be drawn, whose slope is $D_s$. The closer the correlation coefficient ($R^2$) is to 1, the higher the accuracy of the calculated $D_s$.

Figure 10 shows the $D_s$ and $R^2$ values of the porous alumina samples with different pore-forming agent contents. The $D_s$ values of the samples A–D ranged from 2.89673 to 2.61442, and the $R^2$ values were all higher than 0.99000, indicating that the pore distribution of the porous alumina samples was heterogeneous and complex. Therefore, the pore structure of porous alumina has obvious fractal characteristics that can be quantitatively described by the fractal theory. Meanwhile, the $D_s$ values of the porous alumina samples decreased with the increase in the pore-forming agent contents because the contact area between the pore-forming agents and the matrix increased, resulting in fewer small holes and more large holes in the porous alumina samples. Thus, when the $D_s$ value of the pores was larger, the spatial distribution of the material was more complex, and the space-filling capacity was stronger.
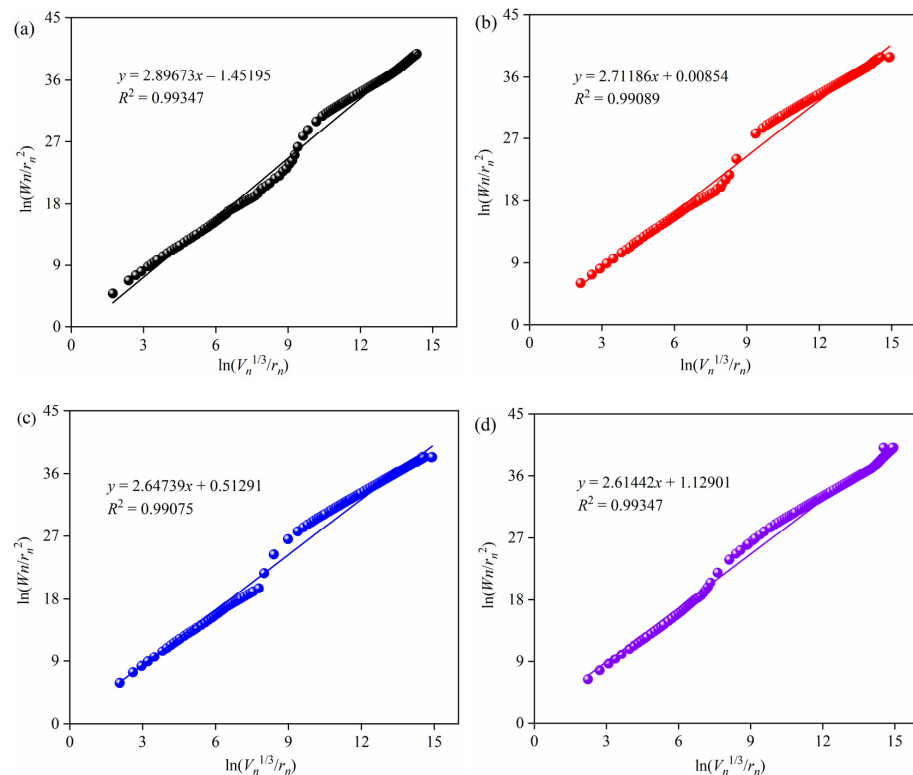


**Figure 10.** Logarithmic plots of $\left(\frac{V_n^{1/3}}{r_n}\right)$ and $\left(\frac{W_n}{r_n^2}\right)$ for samples with different pore-forming agent contents, i.e., (**a**) 20 vol.% pore-forming agents + 80 vol.% alumina; (**b**) 30 vol.% pore-forming agents + 70 vol.% alumina; (**c**) 40 vol.% pore-forming agents + 60 vol.% alumina; (**d**) 50 vol.% pore-forming agents + 50 vol.% alumina.

Figure 11 shows the relationship between $D_s$ and porosity, most probable pore size, and median pore diameter for the porous alumina samples. The porosity, most probable pore size, and median pore diameter decreased as the $D_s$ value increased, with corresponding $R^2$ values of 0.40505, 0.88117, and 0.71016, respectively. As $D_s$ increased, the most probable pore size and the median pore diameter decreased, indicating that the number of small pores increased and the distribution of the pores was more complex. The $R^2$ value in Figure 11a was not high because of the agglomeration of the two pore-forming agents during the sintering process, resulting in an obvious change in the pore surface area with the increase in the pore-forming agent content.
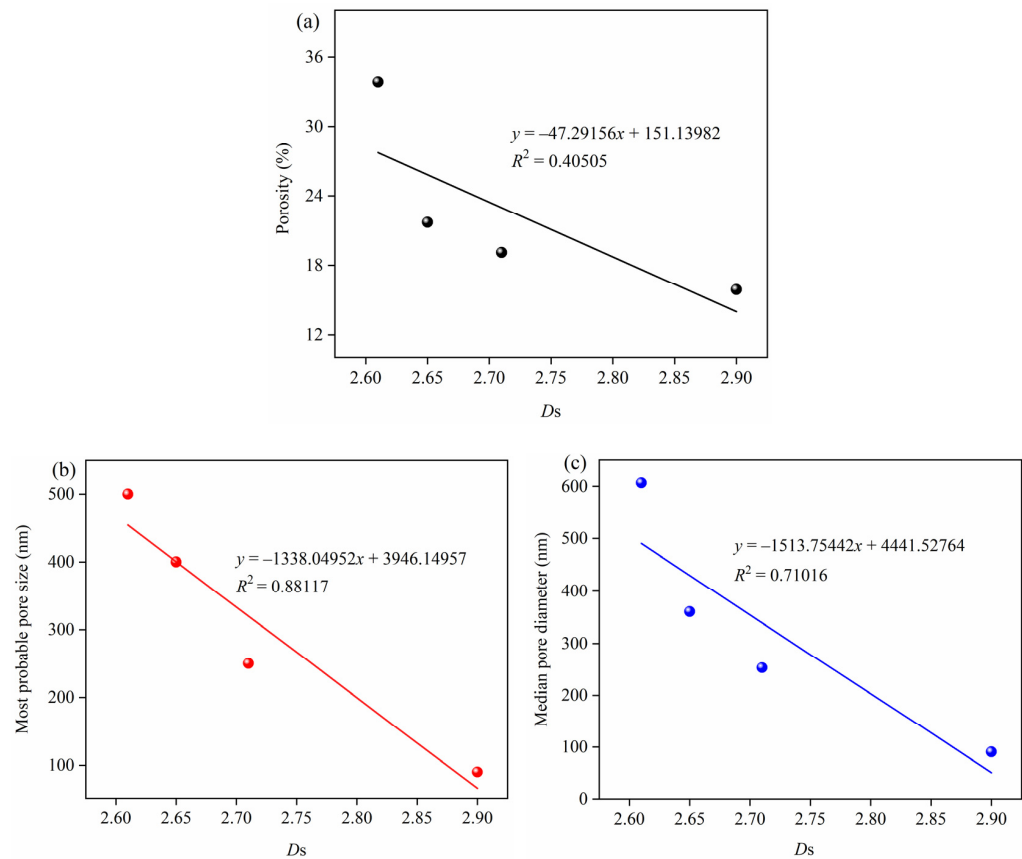


**Figure 11.** Relationship between $D_s$ and (**a**) porosity, (**b**) most probable pore size, and (**c**) median pore diameter of porous alumina.

Figure 12 shows the relationship between bending strength and porosity measured by MIP, most probable pore size, median pore size, and $D_s$ of the porous alumina samples. The bending strength of the samples decreased with the increase in porosity, most probable pore size, and median pore diameter but increased with the increase in the $D_s$ value. The pore area is an important factor affecting the mechanical properties of porous ceramics. It is negatively correlated with density because the pores reduce the effective cross-sectional area of alumina ceramics, reducing their ability to bear a load and resist deformation. Furthermore, the pore shapes formed during the sintering process differed depending on the pore-forming agent content, which also affected the bending strength. With the increase in the $D_s$ value, the density of the samples increased, the pores became more complex, the number of small pores increased, and the mechanical properties of the samples increased.
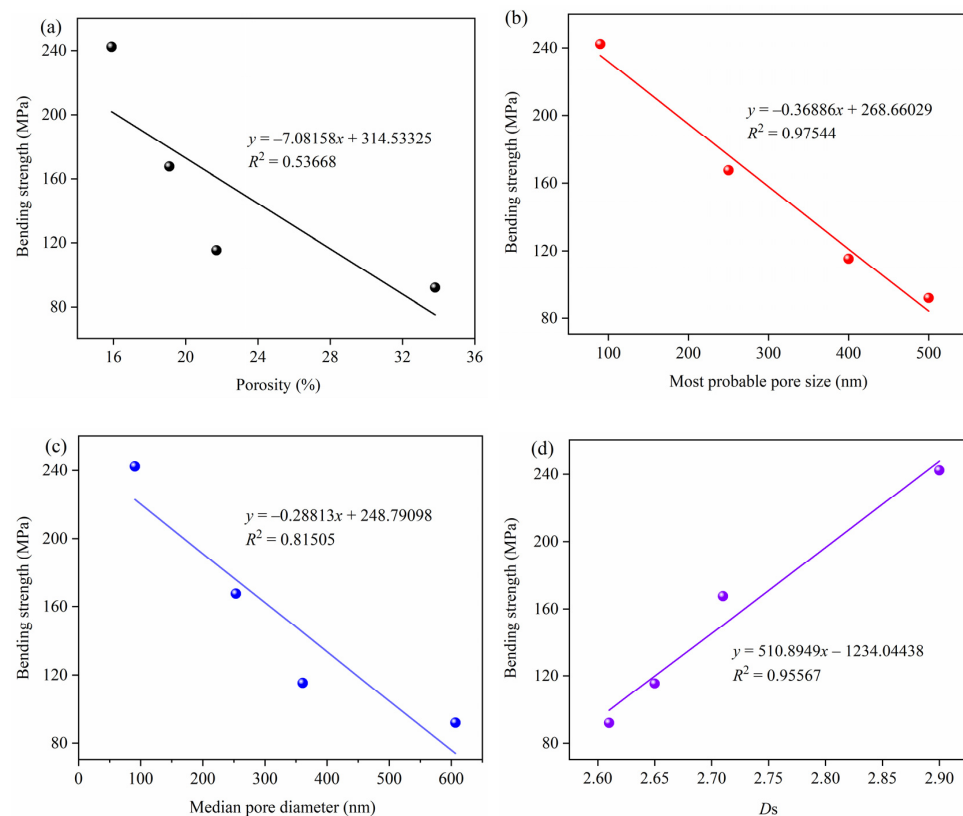
**Figure 12.** Relationship between bending strength and (**a**) porosity, (**b**) most probable pore size, (**c**) median pore diameter of the porous alumina, and (**d**) $D_s$.

## 4. Conclusions

Porous alumina materials were successfully prepared using 20–50 vol.% starch and carbon fibers as the pore-forming agents. The structure and microstructure of porous alumina were closely related to the content of the pore-forming agents. With the increase in the pore-forming agent content, the porosity of porous alumina increased, the number of pores decreased, the pore structure became simple, and the density and mass loss rate decreased. When the pore structure and microstructure changed, the bending strength of the porous alumina decreased as the porosity increased. The pore structure parameters could be described by the $D_s$. The $D_s$ values of the four samples were between 2.61442 and 2.89673, and all $R^2$ values were higher than 0.99000, showing good fractal characteristics. The $D_s$ value decreased with an increasing pore-forming agent content. The values of $D_s$ and bending strength of the porous alumina samples decreased with increasing porosity, most probable pore size, and median pore diameter. The $D_s$ value of porous alumina was positively correlated with the bending strength. Our results provide an experimental basis for evaluating the pore structure and mechanical properties of porous materials.

## References

1. Wang, S.Y.; Yang, Z.; Luo, X.D.; Qi, X.; Zhang, L.; You, J.G. Preparation of calcium hexaluminate porous ceramics by gel–casting method with polymethyl methacrylate as pore–forming agent. *Ceram. Int.* **2022**, *48*, 30356–30366. [CrossRef]
2. Wang, L.L.; Ma, B.Y.; Ren, X.M.; Yu, C.; Deng, C.J.; Liu, C.M.; Hu, C.B. $ZrO_2$ and $M_xO_y$ (M = La, Ce, and Nb) synergistically reinforced porous cordierite ceramics synthesized via a facile solid–state reaction. *Ceram. Int.* **2022**, *27*, R713–R715. [CrossRef]
3. Ohji, T.; Fukushima, M. Macro–porous ceramics: Processing and properties. *Int. Mater. Rev.* **2013**, *57*, 115–131. [CrossRef]
4. Ha, J.H.; Lee, S.J.; Park, B.; Lee, J.; Song, I.H. Feasibility of as–prepared reticulated porous barium titanate without additional radar–absorbing material coating in potential military applications. *J. Aust. Ceram. Soc.* **2020**, *56*, 1481–1491. [CrossRef]
5. Çelik, A.; Çağlar, G.; Çelik, Y. Fabrication of porous $Al_2O_3$ ceramics using carbon black as a pore forming agent by spark plasma sintering. *Ceram. Int.* **2022**, *48*, 28181–28190. [CrossRef]
6. Zhao, D.; Su, H.J.; Liu, Y.; Shen, Z.L.; Liu, H.F.; Guo, Y.N.; Li, X.; Dong, D.; Jiang, H.; Liu, C.C.; et al. Ultrahigh–strength porous ceramic composites via a simple directional solidification process. *Nano Lett.* **2022**, *22*, 2405–2411. [CrossRef] [PubMed]
7. Wang, Y.X.; Zhu, S.F.; Zhou, X.Z.; Zhang, T. Effect of sintering process on micro–structure and properties of mullite porous ceramics containing magnesium oxide. *J. Phys. Conf. Ser.* **2022**, *2206*, 012037. [CrossRef]
8. Pia, G.; Casnedi, L.; Ionta, M.; Sanna, U. On the elastic deformation properties of porous ceramic materials obtained by pore–forming agent method. *Ceram. Int.* **2015**, *41*, 11097–11105. [CrossRef]
9. Loca, D.; Narkevica, I.; Ozolins, J. The effect of $TiO_2$ nanopowder coating on in vitro bioactivity of porous $TiO_2$ scaffolds. *Mater. Lett.* **2015**, *159*, 309–312. [CrossRef]
10. Liu, R.P.; Xu, T.T.; Wang, C.A. A review of fabrication strategies and applications of porous ceramics prepared by freeze–casting method. *Ceram. Int.* **2016**, *42*, 2907–2925. [CrossRef]
11. Huo, W.L.; Zhang, X.Y.; Chen, Y.G.; Hu, Z.L.; Wang, D.; Yang, J.L. Ultralight and high–strength bulk alumina/zirconia composite ceramic foams through direct foaming method. *Ceram. Int.* **2019**, *45*, 1464–1467. [CrossRef]
12. Falsetti, L.O.Z.; Ferreira Muche, D.N.; Santos Junior, T.; Pandolfelli, V.C. Thermodynamics of smart bubbles: The role of interfacial energies in porous ceramic production and non-metallic inclusion removal. *Ceram. Int.* **2021**, *47*, 14216–14225. [CrossRef]
13. Dang, W.; Wang, W.H.; Wu, P.F.; Li, F.P.; Zhao, K.; Tang, Y.F. Freeze-cast porous $Al_2O_3$ ceramics strengthened by up to 80% ceramics fibers. *Ceram. Int.* **2022**, *48*, 9835–9841. [CrossRef]
14. Zhang, C.; Liang, Y.D.; Cui, Z.J.; Meng, F.W.; Zhao, J.; Yu, T.B. Study on the effect of ultrasonic vibration–assisted polishing on the surface properties of alumina ceramic. *Ceram. Int.* **2022**, *48*, 21430–21447. [CrossRef]
15. Zhang, A.; Sang, K.Z.; Zeng, D.J.; Liu, Q.; Guo, Y.J. Preparation and properties of porous alumina with inter–locked platelets structure. *Ceram. Int.* **2022**, *48*, 25918–25922. [CrossRef]
16. Zang, W.J.; Guo, F.; Liu, J.C.; Du, H.Y.; Hou, F.; Guo, A.R. Lightweight alumina based fibrous ceramics with different high temperature binder. *Ceram. Int.* **2016**, *42*, 10310–10316. [CrossRef]
17. Qian, C.C.; Hu, K.H.; Wang, H.Y.; Nie, L.; Feng, Q.; Lu, Z.G.; Li, P.J.; Lu, K. The effect of particle size distribution on the microstructure and properties of $Al_2O_3$ ceramics formed by stereolithography. *Ceram. Int.* **2022**, *48*, 21641–21650. [CrossRef]
18. Wang, Y.; Yan, B.J.; Zhang, Y.X.; Deng, T.F. Fundamental research on the densification of alumina ceramics by ferrotitanium slag. *J. Sustain. Metall.* **2022**, *8*, 122–134. [CrossRef]
19. Bian, H.M.; Yang, Y.; Wang, Y.; Tian, W.; Jiang, H.F.; Hu, Z.J.; Yu, W.M. Effect of microstructure of composite powders on microstructure and properties of microwave sintered alumina matrix ceramics. *J. Mater. Technol.* **2013**, *29*, 429–433. [CrossRef]
20. Hedayat, N.; Du, Y.H.; Ilkhani, H. Review on fabrication techniques for porous electrodes of solid oxide fuel cells by sacrificial template methods. *Renew. Sustain. Energy Rev.* **2017**, *77*, 1221–1239. [CrossRef]
21. Lukacs, V.A.; Stanculescu, R.; Curecheriu, L.; Ciomaga, C.E.; Horchidan, N.; Cioclea, C.; Mitoseriu, L. Structural and functional properties of $BaTiO_3$ porous ceramics produced by using pollen as sacrificial template. *Ceram. Int.* **2020**, *46*, 523–530. [CrossRef]
22. Chen, Y.; Wang, N.N.; Ola, O.; Xia, Y.D.; Zhu, Y.Q. Porous ceramics: Light in weight but heavy in energy and environment technologies. *Mat. Sci. Eng. R Rep.* **2021**, *143*, 100589. [CrossRef]
23. Talou, M.H.; Camerucci, M.A. Processing of porous mullite ceramics using novel routes by starch consolidation casting. *J. Eur. Ceram. Soc.* **2015**, *35*, 1021–1030. [CrossRef]
24. Lorente-Ayza, M.M.; Sánchez, E.; Sanz, V.; Mestre, S. Influence of starch content on the properties of low–cost microfiltration ceramic membranes. *Ceram. Int.* **2015**, *41*, 13064–13073. [CrossRef]
25. Lorente-Ayza, M.M.; Mestre, S.; Sanz, V.; Sánchez, E. On the underestimated effect of the starch ash on the characteristics of low cost ceramic membranes. *Ceram. Int.* **2016**, *42*, 18944–18954. [CrossRef]
26. Ishii, K.; Shimizu, M.; Sameshima, H.; Samitsu, S.; Ishigaki, T.; Uchikoshi, T. Fabrication of porous $(Ba,Sr)(Co,Fe)O_3 - \delta$ (BSCF) ceramics using gelatinization and retrogradation phenomena of starch as pore–forming agent. *Ceram. Int.* **2020**, *46*, 13047–13053. [CrossRef]
27. Zhao, P.C.; Hu, K.H.; Wang, H.Y.; Li, X.Y.; Lu, Z.G. Effect of organic fibers addition on digital light processing for $Al_2O_3$ porous ceramics. *Ceram. Int.* **2021**, *47*, 23144–23152. [CrossRef]
28. Corradetti, S.; Biasetto, L.; Innocentini, M.D.M.; Carturan, S.; Colombo, P.; Andrighetto, A. Use of polymeric fibers to increase gas permeability of lanthanum carbide based targets for nuclear physics applications. *Ceram. Int.* **2016**, *42*, 17764–17772. [CrossRef]
29. Biggemann, J.; Stumpf, M.; Fey, T. Porous alumina ceramics with multimodal pore size distributions. *Materials* **2021**, *14*, 3294. [CrossRef]

30. Zhong, Z.X.; Zhang, B.; Tian, Z.Y.; Ye, J.; Zhang, H.Q.; Gao, Y.; Liu, Q.; Zhang, Z.G.; Ye, F. Highly porous LAS–SiC ceramic with near–zero thermal expansion prepared via aqueous gel–casting combined with adding pore–forming agents. *Mater. Charact.* **2022**, *187*, 111829. [CrossRef]

31. Zeng, Q.; Luo, M.Y.; Pang, X.Y.; Li, L.; Li, K.F. Surface fractal dimension: An indicator to characterize the microstructure of cement–based porous materials. *Appl. Surf. Sci.* **2013**, *282*, 302–307. [CrossRef]

32. Poyet, S. Water transport properties of virtual fractal porous media: Implications for the unsaturated transport properties of cement–based material. *Cem. Concr. Res.* **2021**, *150*, 106613. [CrossRef]

33. Wang, L.; Zeng, X.M.; Yang, H.; Lv, X.D.; Guo, F.X.; Shi, Y.; Hanif, A. Investigation and application of fractal theory in cement–based materials: A review. *Fractal Fract.* **2021**, *5*, 247. [CrossRef]

34. Wang, L.; Jin, M.M.; Wu, Y.H.; Zhou, Y.X.; Tang, S.W. Hydration, shrinkage, pore structure and fractal dimension of silica fume modified low heat Portland cement–based materials. *Constr. Build. Mater.* **2021**, *272*, 121952. [CrossRef]

35. Yang, X.; Zhang, R.J.; Ma, S.; Yang, X.C.; Wang, F.L. Fractal dimension of concrete meso–structure based on X–ray computed tomography. *Powder Technol.* **2019**, *350*, 91–99. [CrossRef]

36. Lan, X.L.; Zeng, X.H.; Zhu, H.S.; Long, G.C.; Xie, Y.J. Experimental investigation on fractal characteristics of pores in air–entrained concrete at low atmospheric pressure. *Cem. Concr. Compos.* **2022**, *130*, 104509. [CrossRef]

37. Yang, H.M.; Zhang, S.M.; Wang, L.; Chen, P.; Shao, D.K.; Tang, S.W.; Li, J.Z. High-ferrite portland cement with slag: Hydration, microstructure, and resistance to sulfate attack at elevated temperature. *Cem. Concr. Compos.* **2022**, *130*, 104560. [CrossRef]

38. Peng, Y.; Tang, S.; Huang, J.; Tang, C.; Wang, L.; Liu, Y. Fractal analysis on pore structure and modeling of hydration of magnesium phosphate cement paste. *Fractal Fract.* **2022**, *6*, 337. [CrossRef]

39. Meng, Q.; Qin, Q.; Yang, H.; Zhou, H.; Wu, K.; Wang, L. Fractal characteristics of the pore structure of coral powder-cement slurry under different fractal models. *Fractal Fract.* **2022**, *6*, 145. [CrossRef]

40. Wang, L.; Zhou, S.; Shi, Y.; Huang, Y.; Zhao, F.; Huo, T.; Tang, S. The influence of fly ash dosages on the permeability, pore structure and fractal features of face slab concrete. *Fractal Fract.* **2022**, *6*, 476. [CrossRef]

41. Li, D.; Niu, D.T.; Fu, Q.; Luo, D.M. Fractal characteristics of pore structure of hybrid Basalt–Polypropylene fibre–reinforced concrete. *Cem. Concr. Compos.* **2020**, *109*, 103555. [CrossRef]